PWM Plus Phase Angle Shift (PPAS) Control Scheme for Combined Multiport DC/DC Converters

Wuhua Li, *Member, IEEE*, Jianguo Xiao, Yi Zhao, *Student Member, IEEE*, and Xiangning He, *Fellow, IEEE*

Abstract—Multiport dc/dc converters are widely employed in hybrid energy generation systems to provide stable power to key loads with high power density. In this paper, the switch duty cycle and the phase angle of the interleaved converters are employed as two control freedoms to achieve decoupled voltage regulation within a certain operating range among different ports, which is referred to as pulsewidth modulation plus phase angle shift (PPAS) control scheme. An interleaved bidirectional buck–boost converter and a full-bridge converter are integrated together to derive a combined three-port dc/dc converter for photovoltaic (PV)-battery hybrid energy systems, which is adopted as a typical example to explore the clear performance of the proposed PPAS control strategy. The bidirectional buck–boost converter and the full-bridge converter share the same power MOSFETs in the primary side, which simplifies the circuit structure and improves the power density. The duty cycle of the interleaved bidirectional buck–boost converter is adopted to realize the maximum power point tracking and the voltage balance between the battery and the PV cell in the primary side. Furthermore, the phase angle of the interleaved buck–boost converter is employed as another control freedom to achieve accurate secondary output voltage regulation. Finally, a 100-W PV-Battery energy system is designed and tested to verify the effectiveness of the proposed scheme.

Index Terms—Combined multiport converter, decoupled control, hybrid energy system, pulsewidth modulation (PWM) plus phase angle shift.

I. INTRODUCTION

SOLAR energy fluctuates during the day and vanishes at night. Therefore, it cannot be considered as a steady energy source for the key load or the grid [1], [2]. However, a photovoltaic (PV)-battery hybrid energy system can overcome the intermittent nature of solar energy and provide reliable power. This calls for two dc/dc converters or a three-port converter to interface the PV array, the battery, and the load. The conventional PV-battery hybrid system requires two individual converters. One converter is used to achieve the PV energy conversion and the other one is employed to charge or discharge the battery. This complex configuration contains many component numbers, increases the system volume and cost. Actually, the two individual

converters can be replaced by a three-port converter to improve the power density.

A parallel structure of several individual bidirectional buck–boost converters is combined for multiport dc/dc conversion systems in [3] and [4]. However, the power devices cannot be shared by different individual converters. By employing the time-sharing control strategy, a multiple-input nonisolated buck–boost converter and its isolated counterparts with unidirectional power flow are proposed in [5] and [6]. Furthermore, some improved multiple-input topologies with multidirectional energy conversion are introduced in [7]. These converters can be easily extended to any number of input ports. Unfortunately, the power devices and the magnetic components have to sustain the peak voltage and current stresses. And the output energy of each port is coupled and difficult to manage due to the time-sharing control scheme. By integrating the half-bridge converter and the active-clamp forward converter, a trimodal half-bridge converter for a three-port interface is presented in [8] and [9]. The component numbers and the power losses can be saved for the power-harvesting systems. However, the control variables of two duty cycles are interactional, which increases the control complexity. This concept can also be extended to four-port even higher port converters [10]. In addition, general rules are carried out to derive nonisolated and isolated multiple-input converters from the single-input versions in [11]–[13], which are adopted to identify the feasible input cell that complies with some assumptions and conditions. The common feature of the aforementioned multiport converters is that the energy management or the control scheme is part coupled or interrestrictive.

Another universal solution to generate multiport converters is to combine the dc-link configuration and adopt the magnetic-coupling solution [14]–[19]. Half-bridge structure, full-bridge structure, and their integration can be employed to satisfy some stringent requirements. The clear advantages of the fully coupled multiport converters are zero-voltage switching (ZVS) operation, easy energy management, and flexible configuration. Phase-shift control scheme or pulsewidth modulation (PWM) plus phase shift control strategy is usually used in these cases. Furthermore, series resonance control scheme can be also employed [20]. However, the variable frequency operation increases the ElectroMagnetic Interference (EMI) filter design difficulty. The main limitation of the fully coupled multiport converters is that a lot of power devices are required because each port cannot share the same power switches.

In order to improve the device sharing ratio among different ports, realize soft-switching operation, and achieve decoupled control within a certain operating range, a novel PWM plus phase angle shift (PPAS) control scheme is proposed in this
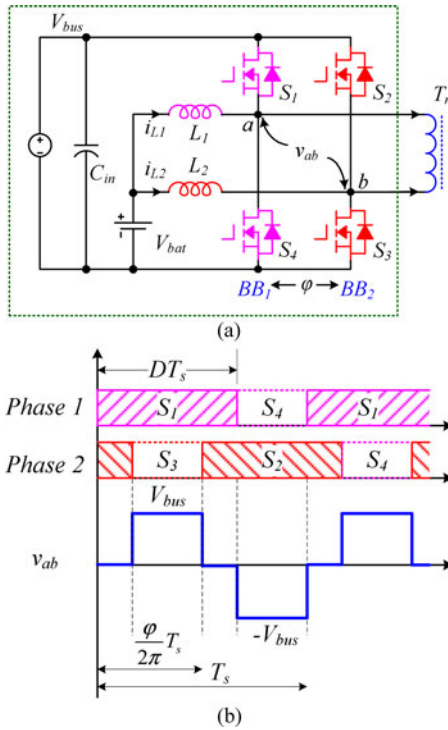
Fig. 1.　Proposed PPAS control scheme. (a) Interleaved bidirectional buck–boost converter. (b) Key steady-state waveforms.

Fig. 2.　Derived combined three-port dc/dc converter.

paper. The bidirectional buck–boost converter and the full-bridge converter are integrated to generate a combined three-port converter for the PV-battery hybrid energy system, which is used as an example to show the operation principle of the proposed PPAS control scheme. The primary power MOSFETs are shared by the bidirectional buck–boost converter and the full-bridge converter to simplify the circuit structure. The switch duty cycle is adopted to achieve the maximum power point tracking (MPPT) performance and balance the voltages between the battery and the PV cells. Furthermore, the phase angle of the interleaved buck–boost converter is employed as another control freedom to regulate the secondary output voltage. As a result, great control flexibility is provided.

II. DERIVATION METHODOLOGY OF THE PPAS CONTROL SCHEME

In order to make a clear picture on accurately illustrating the innovative methodology and easily explaining the operation principle of the proposed PPAS control scheme, the conventional interleaved buck–boost converter is employed as a typical example, which is plotted in the dashed block in Fig. 1(a), where L_1 and L_2 are the filter inductors; S_1, S_2, S_3, and S_4 are the power MOSFETs; C_{in} is the high side capacitor; V_{bus} and V_{bat} are the high and low side voltages, respectively; i_{L1} and i_{L2} are defined as the inductor currents; and v_{ab} is the phase voltage difference of the phase legs BB_1 and BB_2. The steady-state waveforms of the proposed PPAS scheme are introduced in Fig. 1(b), where D is the duty cycle of the upper switches S_1 and S_2, T_s is the switching period, and φ is the phase angle between BB_1 and
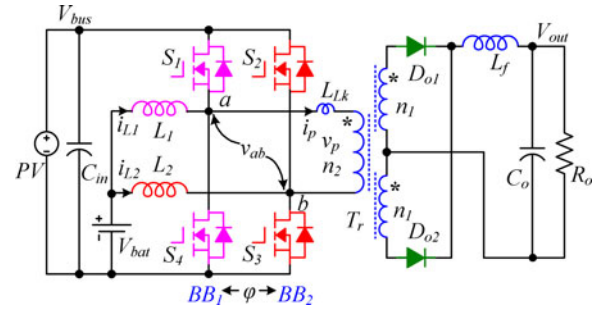
BB_2. In conventional interleaved converters, D is employed as the only control freedom to accurately balance the voltages V_{bus} and V_{bat}. And φ is kept as constant 180° to reduce the current ripple. In the proposed PPAS control strategy, the phase angle φ is adopted as another control freedom to achieve a third voltage regulation in the three-port dc/dc converters. Once φ is adjusted during a selected range, the phase voltage difference v_{ab} varies correspondingly as shown in Fig. 1(b). As a result, a transformer can be inserted into the two phases of the interleaved bidirectional converter to realize another voltage regulation in the secondary side.

III. OPERATION ANALYSIS OF THE DERIVED THREE-PORT CONVERTER

A three-port dc/dc converter for a PV-battery hybrid energy system is derived as an example to explore the advantages of the proposed PPAS control scheme. The circuit configuration of the primary side is the same as shown in Fig. 1(a). The center-tapped rectifier structure is adopted in the secondary side. The combined three-port converter is illustrated in Fig. 2. Other rectifier configurations, such as full-bridge rectifier, current-double rectifier, and so on, can be also applied to the combined converter to satisfy various application requirements [21], [22]. In the PV-battery hybrid energy system, the PV array with unidirectional power flow and the battery are interfaced with BB_1 and BB_2 with bidirectional power flow. The PWM control strategy of the interleaved buck–boost converter is employed to realize MPPT performance and control the battery state of charge (SOC). In addition, the switches S_1, S_2, S_3 and S_4; the center-tapped transformer T_r; the output diodes D_{o1} and D_{o2}; the output filter inductor L_f; and the output capacitor C_o compose a full-bridge converter, which can deliver energy to the secondary load. The phase angle shift control strategy is employed to regulate the output voltage. The combined three-port dc/dc converter is an integration of the bidirectional buck–boost converter and a full-bridge converter, which share the same power switches. As a result, the power density is improved and the cost is reduced. It should be noted that the duty cycle of the switches is variable rather than fixed for the built-in full-bridge converter compared with the conventional phase-shift full-bridge converter. The transformer T_r can be equivalent to a leakage inductor L_{Lk} in series with an ideal transformer. The primary winding of the transformer is n_2 turns. The second and third windings are both
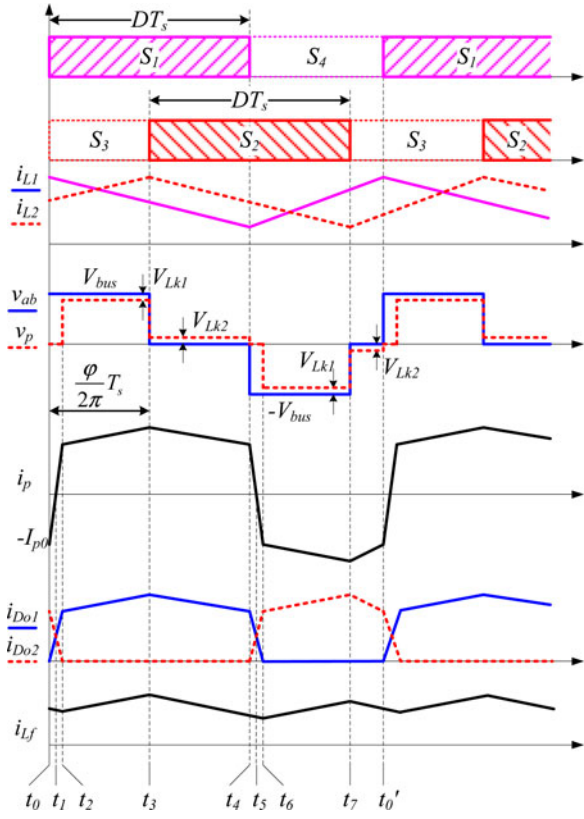
Fig. 3. Key waveforms in battery discharging mode.

n_1 turns. The turns ratio N is defined as n_2/n_1. The coupling reference is marked by "∗." As shown in Fig. 2, v_p is the magnetizing inductor voltage of T_r and V_{out} is the secondary output voltage of the combined three-port converter.

In order to simplify the circuit operation analysis, the magnetizing inductor of the transformer is assumed to be infinite and all the power devices are ideal. There are two operation modes for the battery. One is the battery charging mode and the other is the battery discharging mode. The key steady-state waveforms in the battery discharging mode are shown in Fig. 3. Once in the battery charging mode, all of the waveforms are nearly the same except that the inductor currents i_{L1} and i_{L2} change their directions. Therefore, only the battery discharging mode is analyzed here. There are eight operational stages in one switching period. The corresponding equivalent circuits are shown in Fig. 4.

Stage 1 [t_0–t_1] [see Fig. 4(a)]: At t_0, S_1 is turned ON and S_3 remains in ON state. L_1 is discharged and L_2 is still charged linearly. The phase voltage difference v_{ab} is V_{bus}. The leakage inductor current i_p increases from the initial value $-I_{p0}$ to zero. Meanwhile, D_{o1} and D_{o2} begin to conduct simultaneously. The magnetizing inductor voltage v_p is zero since the second and third windings are short circuited. The current through D_{o1} decreases while that through D_{o2} increases. This stage ends until i_p is zero

$$i_p(t) = -I_{p0} + \frac{V_{bus}}{L_{Lk}} \cdot t \tag{1}$$

$$t_1 - t_0 = \frac{L_{Lk} \cdot I_{p0}}{V_{bus}}. \tag{2}$$
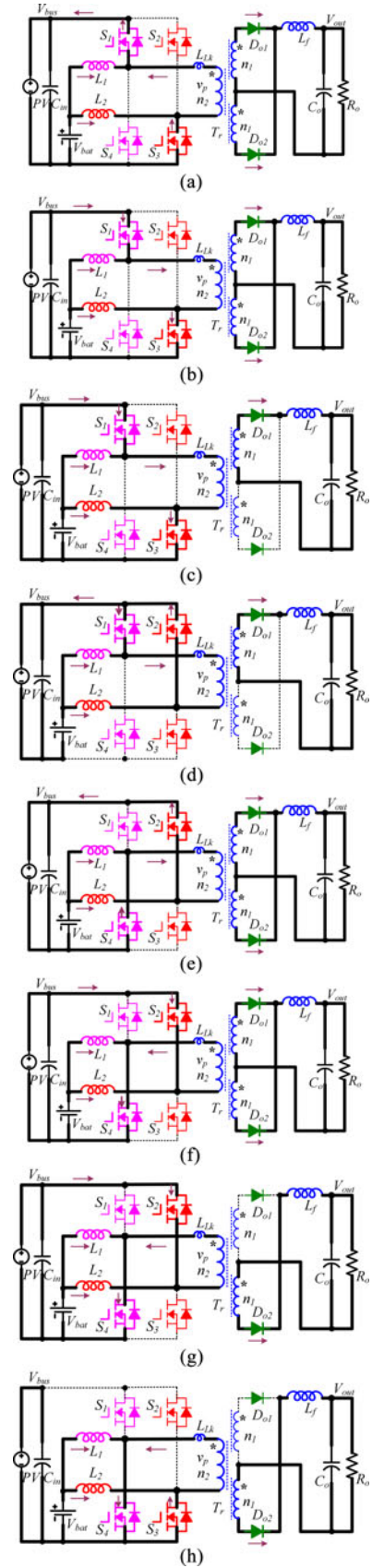
Fig. 4. Operation stages in battery discharging mode. (a) Stage 1 [t_0–t_1]. (b) Stage 2 [t_1–t_2]. (c) Stage 3 [t_2–t_3]. (d) Stage 4 [t_3–t_4]. (e) Stage 5 [t_4–t_5]. (f) Stage 6 [t_5–t_6]. (g) Stage 7 [t_6–t_7]. (h) Stage 8 [t_7–t_0'].

Stage 2 [t_1–t_2] [see Fig. 4(b)]: At t_1, the leakage inductor current i_p increases from zero. The voltages of v_{ab} and v_p and the operational states of all the power devices remain unchanged. The current commutation of D_{o1} and D_{o2} continues until the diode current i_{Do2} decreases to zero while i_{Do1} is equal to the output filter inductor current i_{Lf}

$$i_p(t) = \frac{V_{\text{bus}}}{L_{Lk}} \cdot (t - t_1). \tag{3}$$

Stage 3 [t_2–t_3] [see Fig. 4(c)]: At t_2, D_{o2} is reverse-biased and the output filter inductor current i_{Lf} fully flows through D_{o1}. The leakage inductor current i_p is the output filter inductor current i_{Lf} divided by N. The primary voltage v_{ab} is V_{bus}, but the magnetizing inductor voltage v_p is $(V_{\text{bus}} - V_{Lk1})$, where V_{Lk1} is given by

$$V_{Lk1} \approx \frac{L_{Lk}}{N^2 \cdot L_f} (V_{\text{bus}} - N \cdot V_{\text{out}}) \tag{4}$$

$$i_p(t) = I_p(t_2) + \frac{V_{Lk1}}{L_{Lk}} \cdot (t - t_2). \tag{5}$$

Stage 4 [t_3–t_4] [see Fig. 4(d)]: At t_3, S_3 is turned OFF while S_2 is turned ON. The inductor current i_{L2} starts to decrease and the output filter inductor current begins to freewheel through D_{o1}. The primary voltage v_{ab} is shorted by S_1 and S_2, but the magnetizing inductor voltage v_p is equal to the small value V_{Lk2}, which is derived by

$$V_{Lk2} \approx \frac{L_{Lk}}{N \cdot L_f} \cdot V_{\text{out}} \tag{6}$$

$$i_p(t) = I_p(t_3) - \frac{V_{Lk2}}{L_{Lk}} \cdot \left(t - \frac{\varphi}{2\pi} \cdot T_s\right). \tag{7}$$

Stage 5 [t_4–t_5] [see Fig. 4(e)]: At t_4, S_1 is turned OFF while S_4 is turned ON. The inductor current i_{L1} starts to increase. The leakage inductor current i_p starts to decrease since the primary voltage v_{ab} is $-V_{\text{bus}}$, but the magnetizing inductor voltage v_p is zero. At the same time, D_{o1} and D_{o2} begin to conduct simultaneously. The diode current i_{Do1} decreases and i_{Do2} increases until the leakage inductor current i_p reduces to zero

$$i_p(t) = I_p(t_4) - \frac{V_{\text{bus}}}{L_{Lk}} \cdot (t - D \cdot T_s). \tag{8}$$

Stage 6 [t_5–t_6] [see Fig. 4(f)]: At t_5, the leakage inductor current i_p decreases from zero to a negative value linearly. D_{o1} and D_{o2} are still in the conduction state and the diode current i_{Do1} decreases to zero

$$i_p(t) = -\frac{V_{\text{bus}}}{L_{Lk}} \cdot (t - t_5). \tag{9}$$

Stage 7 [t_6–t_7] [see Fig. 4(g)]: At t_6, D_{o1} is blocked and the output filter inductor current i_{Lf} flows through D_{o2}. The primary voltage v_{ab} is $-V_{\text{bus}}$ and the magnetizing inductor voltage v_p is $(-V_{\text{bus}} + V_{Lk1})$.

Stage 8 [t_7–t_0'] [see Fig. 4(h)]: At t_7, S_2 is turned OFF while S_3 is turned ON. The inductor current i_{L2} starts to increase. The primary voltage v_{ab} is shorted by S_3 and S_4 and the magnetizing inductor voltage v_p equals to $-V_{Lk2}$. This stage ends until S_1 is turned ON. Then, a new switching period begins.

IV. CIRCUIT PERFORMANCE ANALYSIS

A. Formula Derivation

The output filter inductor L_f is assumed to be large enough and its current ripple is ignored to simplify the voltage gain derivation. The secondary inductor current i_{Lf} is equal to the output current I_o. The variation range of the phase angle φ is from zero to π. There are three possible operation cases based on the relationship between the duty cycle D and the phase angle φ, which are shown in Fig. 5.

Case 1 [($\varphi/2\pi$) < D and ($\varphi/2\pi$) < (1 − D)] [see Fig. 5(a)]: During the time interval 0 to T_r, the increment of the leakage inductor current should satisfy the following:

$$\frac{V_{\text{bus}}}{L_{Lk}} \cdot T_r = 2 \cdot \frac{I_o}{N}. \tag{10}$$

The output current can be expressed by

$$I_o = \frac{V_{\text{out}}}{R_o}. \tag{11}$$

Due to the volt-second balance principle on the output filter inductor, the output voltage can be derived by

$$V_{\text{out}} = \frac{1}{T_s} \int_0^{T_s} \frac{|v_p|}{N} dt = \frac{2}{T_s} \cdot \frac{V_{\text{bus}}}{N} \cdot \left(\frac{\varphi}{2\pi} T_s - T_r\right). \tag{12}$$

From (10) to (12), the output voltage is a function of the phase angle φ, which is obtained by

$$V_{\text{out}} = \frac{2V_{\text{bus}}/N}{1 + (4L_{Lk}/N^2 \cdot R_o \cdot T_s)}$$
$$\cdot \frac{\varphi}{2\pi} \left[\frac{\varphi}{2\pi} \leq D \text{ and } \frac{\varphi}{2\pi} \leq (1 - D)\right]. \tag{13}$$

Case 2 [D < 0.5 and D < ($\varphi/2\pi$) < (1 − D)] [see Fig. 5(b)]: Employing the similar derivation procedure, the output voltage can be given by

$$V_{\text{out}} = \frac{1}{T_s} \int_0^{T_s} \frac{|v_p|}{N} dt = \frac{2}{T_s} \cdot \frac{V_{\text{bus}}}{N} \cdot (D \cdot T_s - T_r). \tag{14}$$

Based on (10), (11), and (14), the output voltage is a function of the duty cycle D, which is written by

$$V_{\text{out}} = \frac{2V_{\text{bus}}/N}{1 + (4L_{Lk}/N^2 \cdot R_o \cdot T_s)}$$
$$\cdot D \left[D < 0.5 \text{ and } D < \frac{\varphi}{2\pi} < (1 - D)\right]. \tag{15}$$

Case 3 [D > 0.5 and (1 − D) < ($\varphi/2\pi$) < D] [see Fig. 5(c)]: Applying a similar mathematical derivation, the output voltage is a function of the variable $(1 - D)$, which is given
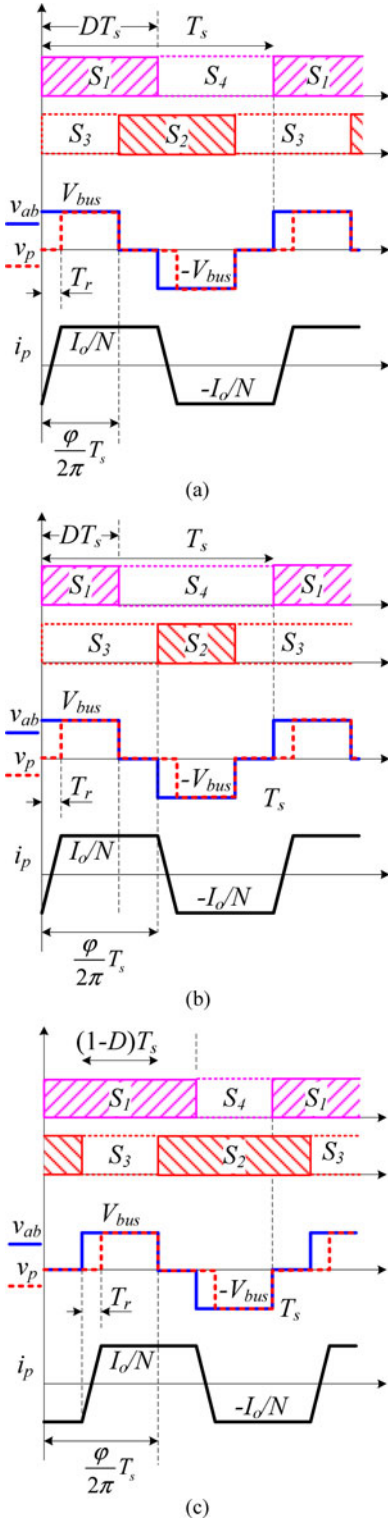
Fig. 5. Three operation modes. (a) $(\varphi/2\pi) < D$ and $(\varphi/2\pi) < (1-D)$. (b) $D < 0.5$ and $D < (\varphi/2\pi) < (1-D)$. (c) $D > 0.5$ and $(1-D) < (\varphi/2\pi) < D$.

by

$$V_{\text{out}} = \frac{2V_{\text{bus}}/N}{1 + (4L_{Lk}/N^2 \cdot R_o \cdot T_s)}$$
$$\cdot (1-D) \left[D > 0.5 \text{ and } (1-D) < \frac{\varphi}{2\pi} < D \right]. \quad (16)$$

As a result, the general output voltage can be summarized by

$$V_{\text{out}} = \begin{cases} G \cdot \dfrac{\varphi}{2\pi} \cdot V_{\text{bus}} & \left[\dfrac{\varphi}{2\pi} \leq D \text{ and } \dfrac{\varphi}{2\pi} \leq (1-D) \right] \\ G \cdot D \cdot V_{\text{bus}} & \left[D < 0.5 \text{ and } D < \dfrac{\varphi}{2\pi} < (1-D) \right] \\ G \cdot (1-D) \cdot V_{\text{bus}} & \left[D > 0.5 \text{ and } (1-D) < \dfrac{\varphi}{2\pi} < D \right] \end{cases} \quad (17)$$

$$G = \frac{2}{N} \cdot \frac{1}{1 + (4L_{Lk}/N^2 \cdot R_o \cdot T_s)}. \quad (18)$$

From the previous analysis, the duty cycle D can be employed to balance the two primary voltages and the phase angle φ is adopted to regulate the secondary output voltage. These two control freedoms make the three-variable system fully controllable. There is a restrictive condition for the combined three-port converter with the proposed PPAS control scheme, which is rewritten by

$$\frac{\varphi}{2\pi} \leq D \text{ and } \frac{\varphi}{2\pi} \leq (1-D). \quad (19)$$

From the general output voltage gain expression shown in (17), it can be determined that the secondary output voltage is determined by the switch duty cycle rather than the phase angle if the restrictive condition cannot be satisfied. This means that the decoupled control performance is lost. As a result, the duty cycle and the phase angle should be limited to an acceptable range. Fortunately, this can be easily implemented by the advanced digital signal processor. During the start-up operation, an open-loop control strategy can be employed before the required voltage is built to guarantee the effective operation.

The primary interleaved buck–boost converter operates in the continuous-conduction mode due to the asymmetrical complementary operation of the upper and lower switches. The relationship between the battery voltage and the bus voltage is derived by

$$V_{\text{bat}} = D \cdot V_{\text{bus}}. \quad (20)$$

From (17) to (20), the restrictive condition among the battery voltage, bus voltage, and secondary output voltage can be obtained by

$$V_{\text{out}} \leq G \cdot V_{\text{bat}} \text{ and } V_{\text{out}} \leq G \cdot (V_{\text{bus}} - V_{\text{bat}}). \quad (21)$$

The voltage stress of the output diodes D_{o1} and D_{o2} is determined by the bus voltage and the turn ratio of the transformer, which is given by

$$V_{Do1} = V_{Do2} = \frac{2V_{\text{bus}}}{N}. \quad (22)$$

Although a small dc current through the transformer primary winding may exist due to the potential mismatch of the switching legs, it is convenient and effective to balance it by inserting a small dc block capacitor into the primary winding, which is a widely employed solution in the conventional phase shift full-bridge converters.
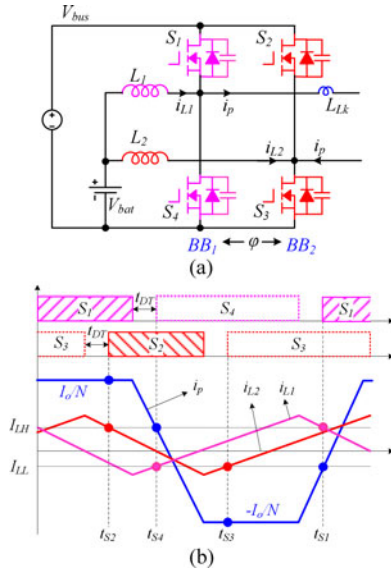
Fig. 6.   Operational waveforms with dead time t_{DT}. (a) Simplified primary circuit. (b) Key waveforms.

B. ZVS Soft-Switching Performance

ZVS soft-switching performance can be achieved due to the phase angle shift control strategy, which is similar to the conventional phase shift full-bridge converter. However, due to the existence of the primary inductors L_1 and L_2, ZVS performance of the combined three-port converter is relatively complicated. ZVS condition of the combined converter is influenced by the following factors: the leakage inductor L_{Lk}, the inductor currents i_{L1} and i_{L2}, the output power of the PV array P_{bus}, the load power P_{out}, the dead time t_{DT}, and the junction capacitance of the switches. By ignoring the current ripple on the output filter inductor L_f, the ideal operation waveforms with an exaggerated dead time t_{DT} are shown in Fig. 6. The currents I_{LH} and I_{LL} represent the peak and valley values of the inductor current i_{L1} or i_{L2} since the dead time is small enough to ignore the inductor current variation during the time interval t_{DT}. The battery discharging operation is employed as an example to discuss the soft-switching operation of the proposed converter. Actually, the ZVS range in the battery charging operation is quite similar to that in the battery discharging operation. The following analytical procedure and results are universal regardless of the operation mode.

Once the antiparallel diode of the MOSFET is in the turn-ON state before its turn-ON gate signal comes, ZVS turn-ON is achieved. Therefore, ZVS conditions of the switches S_1–S_4 can be derived by

$$
\begin{cases}
I_p(t_{S1}) - I_{LH} < 0 & \text{for } S_1 \\
I_p(t_{S2}) + I_{LH} > 0 & \text{for } S_2 \\
I_p(t_{S3}) + I_{LL} < 0 & \text{for } S_3 \\
I_p(t_{S4}) - I_{LL} > 0 & \text{for } S_4
\end{cases}
\tag{23}
$$

where $I_p(t_1)$ to $I_p(t_4)$ are represented by

$$
\begin{cases}
I_p(t_{S1}) = -\dfrac{I_o}{N} + \dfrac{V_{\mathrm{bus}}}{L_{Lk}} \cdot t_{\mathrm{DT}} \\[2mm]
I_p(t_{S2}) = \dfrac{I_o}{N} \\[2mm]
I_p(t_{S3}) = -\dfrac{I_o}{N} \\[2mm]
I_p(t_{S4}) = \dfrac{I_o}{N} - \dfrac{V_{\mathrm{bus}}}{L_{Lk}} \cdot t_{\mathrm{DT}}.
\end{cases}
\tag{24}
$$

From (23) and (24), it can be seen that the ZVS condition of switches S_1 and S_4 is more rigorous than that of switches S_2 and S_3 because the term $(V_{\mathrm{bus}}/L_{Lk}) \cdot t_{\mathrm{DT}}$ is positive. As a result, the ZVS condition of all power MOSFETs can be guaranteed once the following is satisfied

$$
\begin{cases}
I_{LH} > -\dfrac{I_o}{N} + \dfrac{V_{\mathrm{bus}}}{L_{Lk}} \cdot t_{\mathrm{DT}} \\[2mm]
I_{LL} < \dfrac{I_o}{N} - \dfrac{V_{\mathrm{bus}}}{L_{Lk}} \cdot t_{\mathrm{DT}}.
\end{cases}
\tag{25}
$$

From (25), it can be concluded that the ZVS condition is determined by the secondary output current, the turns ratio of the transformer, the bus voltage, the leakage inductor, the dead time, and the current ripple on the primary inductors.

Assuming the circuit conversion efficiency is unity, the peak and the valley current values can be derived by

$$
\begin{cases}
I_{LH} = \dfrac{P_{\mathrm{out}} - P_{\mathrm{bus}}}{2V_{\mathrm{bat}}} + \dfrac{1}{2} \cdot \dfrac{V_{\mathrm{bat}}}{L_1} \cdot (1-D) \cdot T_s \\[2mm]
I_{LL} = \dfrac{P_{\mathrm{out}} - P_{\mathrm{bus}}}{2V_{\mathrm{bat}}} - \dfrac{1}{2} \cdot \dfrac{V_{\mathrm{bat}}}{L_1} \cdot (1-D) \cdot T_s.
\end{cases}
\tag{26}
$$

As a result, the detailed ZVS condition of the combined three-port converter can be represented by

$$
\begin{cases}
P_{\mathrm{bus}} < \left(1 + \dfrac{2V_{\mathrm{bat}}}{N \cdot V_{\mathrm{out}}}\right) \cdot P_{\mathrm{out}} + \dfrac{V_{\mathrm{bat}}^2}{L_1} \cdot (1-D) \cdot T_s \\[2mm]
\qquad\qquad - \dfrac{2V_{\mathrm{bat}} \cdot V_{\mathrm{bus}}}{L_{Lk}} \cdot t_{\mathrm{DT}} \\[3mm]
P_{\mathrm{bus}} > \left(1 - \dfrac{2V_{\mathrm{bat}}}{N \cdot V_{\mathrm{out}}}\right) \cdot P_{\mathrm{out}} - \dfrac{V_{\mathrm{bat}}^2}{L_1} \cdot (1-D) \cdot T_s \\[2mm]
\qquad\qquad + \dfrac{2V_{\mathrm{bat}} \cdot V_{\mathrm{bus}}}{L_{Lk}} \cdot t_{\mathrm{DT}}.
\end{cases}
\tag{27}
$$

From (27), the ZVS margin of the combined converter with a PPAS control scheme is plotted in Fig. 7, where a PV-battery hybrid generation system is employed with the following parameters: $V_{\mathrm{bat}} = 24$ V, $V_{\mathrm{bus}} = 50$ V, $V_{\mathrm{out}} = 12$ V, $L_1 = L_2 = 150~\mu$H, $L_{Lk} = 3~\mu$H, $N = 2$, $t_{\mathrm{DT}} = 50$ ns. A wide-range ZVS operation can be achieved to improve the circuit efficiency.

From (27), it can be concluded that the inductors of the bidirectional buck–boost converter has a minor impact on the ZVS range. The ZVS margin of the combined converter with different inductors is drawn in Fig. 8. ZVS range is extended when the inductors of the bidirectional buck–boost converter decrease. As
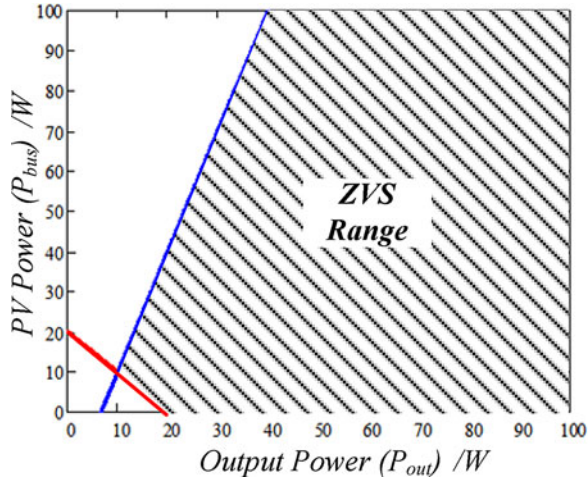
Fig. 7. ZVS margin ($V_{\text{bat}} = 24$ V, $V_{\text{bus}} = 50$ V, $V_{\text{out}} = 12$ V, $L_1 = L_2 = 150 \mu$H, $L_{Lk} = 3 \mu$H, $N = 2$, $t_{\text{DT}} = 50$ ns).
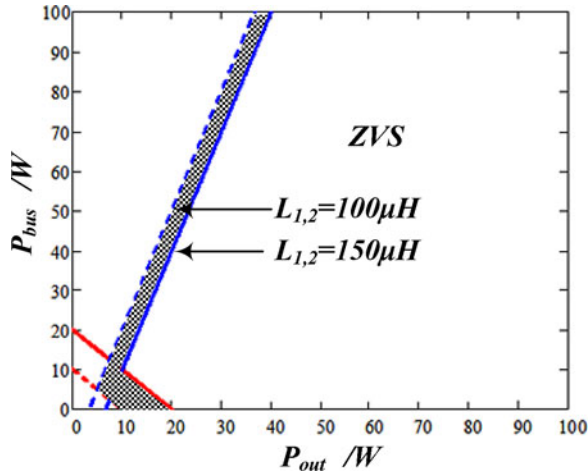

Fig. 8. ZVS margin with different primary inductors ($V_{\text{bat}} = 24$ V, $V_{\text{bus}} = 50$ V, $V_{\text{out}} = 12$ V, $L_{Lk} = 3 \mu$H, $N = 2$, $t_{\text{DT}} = 50$ ns).

a result, the inductor design should be compromised between the ZVS range and the current ripple.

In the aforementioned analysis, the influence of the switch junction capacitance is not demonstrated clearly and directly in (25). In fact, the dead time t_{DT} is determined by the switch junction capacitance, the bus voltage, and the capacitor charging current. The larger the switch junction capacitance, the longer the critical dead time. From (27), it can be concluded that the ZVS soft-switching range is reduced.

C. Topology Extension of Proposed Multiport Converters

The proposed three-port converter with the PPAS control strategy can be extended to other multiport converters. This extension concept can be divided into two parts. The first one is the extension on the primary ports as shown in Fig. 9(a) and the other one is the extension on the secondary ports as plotted in Fig. 9(b). The battery shown in Fig. 1(a) can be separated into two similar distributed cells to achieve a four-port converter, which can improve the battery usage life and enhance the sys-
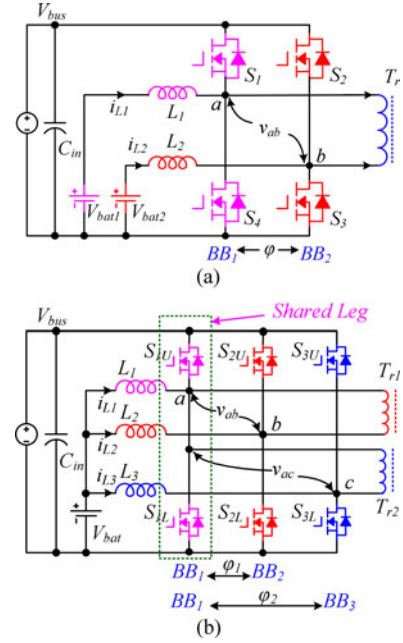

Fig. 9. Extension of the proposed multiport converters. (a) Extension of primary ports. (b) Extension of secondary ports.

tem reliability. Furthermore, there are only two half-bridge legs in the proposed converter. However, the numbers of the half-bridge legs are not limited. Another bridge leg and transformer can be inserted to produce a fourth port as shown in Fig. 9(b). One of the half-bridge legs serves as the shared leg. A general principle is that $(M-1)$ secondary output ports can be produced by employing M half-bridge legs.

V. FEEDBACK CONTROL LOOP DESIGN

The control block diagram of the combined three-port converter for the PV-battery hybrid power generation system is introduced in Fig. 10. The switch duty cycle of the interleaved buck–boost converter is employed to keep the voltage balance between the PV array and the battery, achieve MPPT performance, and realize battery SOC management. Control loop 1 is for battery charging or discharging realization. Control loop 2 is for MPPT achievement. There are a lot of advanced MPPT solutions presented in the recent papers to improve PV efficiency [23]–[26]. Most of them can be applied in the proposed PV-battery hybrid system. Only the simplest open-circuit voltage MPPT method is adopted here because this paper mainly focuses on clear performance analysis on the proposed PPAS scheme. The primary current control loop can not only achieve the battery charging and discharging states control, but also realize current sharing between the two phases of the bidirectional buck–boost converter. The two diodes shown in Fig. 10 can serve as a smart switch to select the proper control loop based on the PV-battery-load state [27]. For example, when the battery voltage is lower than the floating voltage, the output of loop 1 is high to make the diode D_{L1} reverse-biased and the primary switch duty cycle is controlled by the MPPT loop to make full use of the PV energy. Once the battery voltage reaches
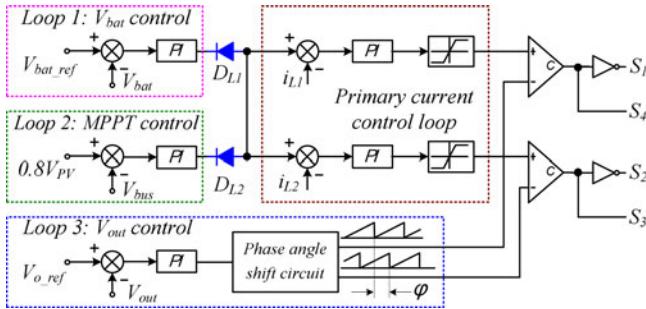
Fig. 10. Control loop of combined three-port converter.

TABLE I
PROTOTYPE SPECIFICATIONS

Bus voltage (V_{bus})	45~70V
Battery voltage (V_{bat})	20~28V
Secondary output voltage (V_{out})	12V
Switching frequency (f_s)	100kHz
Maximum secondary power (P_{out})	100W

the floating voltage, the diode D_{L1} is turned OFF and the battery voltage control loop is in operation to achieve the constant voltage charging management with a small current. The primary current control loop can achieve the constant current charging once the PV energy is higher than the battery and second load requirements. In this case, the PV cell is no longer in MPPT mode. A trimode PV-battery energy management can be easily achieved [27]. Furthermore, the phase angle is controlled to regulate the output voltage, which is shown as loop 3 in Fig. 10. The phase angle of the saw-tooth waves for modulation is shifted to regulate the output voltage, which can be implemented by the conventional phase shift controller. With the proposed PPAS scheme, the phase angle as another control freedom is provided to achieve decoupled control within a certain operating range for multiport converters, which shows great design flexibility.

VI. PARAMETER DESIGN GUIDELINES

It is known that there is a restrictive condition for the combined three-port converter. From (19), it can be drawn that the phase angle has the maximum variation range when the battery voltage is half of the bus voltage. In this case, the switch duty cycle is approximately 0.5 and the upper limitation of the phase angle is π. A 100-W PV-battery hybrid power generation system operating at 100 kHz switching frequency is adopted as an example to explore the main parameter design considerations. The system specifications are given in Table I.

The duty cycle D of the interleaved bidirectional buck–boost converter varies from 0.36 to 0.62 for the tested prototype. From the aforementioned analysis, the maximum value of the phase angle φ is 130°. The designed phase angle range is from 0 to 120° with 10° margin to guarantee the correct operation.

A. Transformer Design

The design criterion for the transformer is to make sure that the voltage stress of the secondary diodes is in an acceptable scope and the voltage regulation can be achieved within the

expected phase angle range. From (22), it can be drawn that the voltage stress of the secondary diodes is about 70 V when the transformer turns ratio is 2. And with $N = 2$, the required leakage inductance can be derived by

$$L_{Lk} = \frac{N^2 \cdot V_{out}^2}{4f_s \cdot P_{out}} \cdot \left(\frac{2}{N} \cdot \frac{\varphi_{max}}{2\pi} \cdot \frac{V_{bus}}{V_{out}} - 1 \right). \quad (28)$$

The maximum required leakage inductance is 3.6 μH.

B. Inductor Design

The two primary filter inductors L_1 and L_2 should have the same value due to the current sharing balance. The designed primary inductor current ripple is half of its average current considering their influence on the ZVS soft-switching range. As a result, the primary filter inductor value is derived by

$$L_1 = L_2 = \frac{V_{bat} \cdot (1 - D)}{\Delta I_{L1} \cdot f_s} = 153 \ \mu H. \quad (29)$$

The secondary filter inductor L_f is designed to make that the secondary current ripple is 10% of the average output current, which is derived by

$$L_f = \frac{V_{out} \cdot (D_{max} - (\varphi_{min}/2\pi))}{\Delta I_{Lf} \cdot f_s} = 20.7 \ \mu H. \quad (30)$$

C. Power Device Selection

The voltage stress of the primary switches and secondary diodes can be carried out from the aforesaid voltage stress analysis. In this case, IRF540Z (100 V at 36 A) is selected as the primary switch and MBR30H100CT (100 V at 30 A) is employed as the secondary output diode. The dead time t_{DT} is selected as 50 ns to achieve ZVS soft-switching performance under a certain load condition based on the detailed analysis in Fig. 8.

VII. EXPERIMENTAL VERIFICATION

A 100-W prototype is designed and built to verify the effectiveness of the proposed PPAS scheme.

The steady-state waveforms on the battery discharging mode are shown in Fig. 11. In this case, the secondary load is 100 W, the PV output power is about 50 W, and the rest energy is provided by the battery. This means that both the PV array and the battery transfer their energy to the load to achieve the three-port conversion. It can be seen that the average currents of the inductors L_1 and L_2 are equal due to the current sharing control loop. As the duty cycle varies, the low and high side voltages of the bidirectional buck–boost converter can be balanced. And the phase angle is shifted as the secondary side load changes. The magnetizing inductor voltage v_p in Fig. 11(b) is the equivalent voltage from the second winding because it cannot be measured directly due to the built-in transformer.

The ZVS turn-ON waveforms of the switches S_1 an S_4 are shown in Fig. 12. Due to the circuit symmetry, the two upper switches S_1 and S_2 have similar soft-switching performance and the two bottom switches S_3 and S_4 operate with similar performance. It can be seen that the switch drain-source voltage decreases to zero before its turn-ON gate signal comes at the
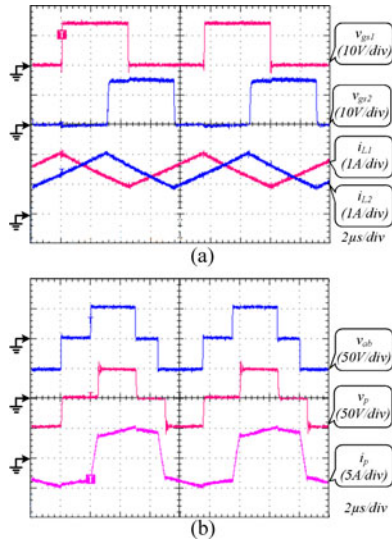
Fig. 11. Steady-state waveforms with $V_{bus} = 50\,V$, $V_{bat} = 24\,V$, $P_{bus} = 50\,W$, $P_{out} = 100\,W$. (a) Effect of current sharing loop. (b) Phase angle shift waveforms.
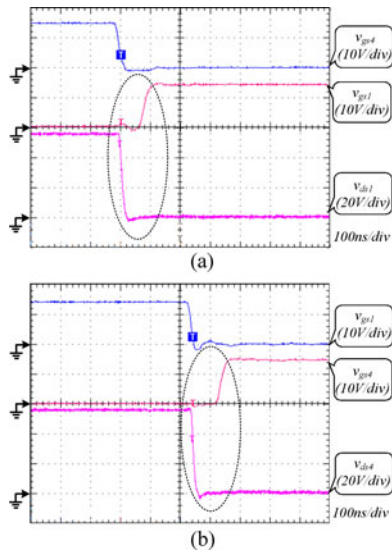

Fig. 12. ZVS-ON performance $V_{bus} = 55\,V$, $V_{bat} = 20\,V$, $P_{bus} = 55\,W$, $P_{out} = 60\,W$. (a) ZVS-ON waveforms of S_1. (b) ZVS-ON waveforms of S_4.

Fig. 13. Critical ZVS-ON performance $V_{bus} = 55\,V$, $V_{bat} = 20\,V$, $P_{bus} = 10\,W$, $P_{out} = 12\,W$. (a) ZVS-ON waveforms of S_1. (b) ZVS-ON waveforms of S_4.

Fig. 14. Dynamic response of combined three-port converter with $V_{bus} = 50\,V$, $V_{bat} = 24\,V$, $P_{bus} = 50\,W$. (a) Voltage waveforms with ac coupling. (b) Current waveforms.

measured load. As a result, ZVS soft-switching performance is achieved for all the primary power MOSFETs to reduce the switching losses.

The critical ZVS operation range of the combined three-port dc/dc converter with the proposed PPAS scheme is plotted in Fig. 13. When the PV output power is 10 W and the secondary load is 12 W, the drain-source voltage of the switch S_1 is just reduced to zero at the interval that its turn-ON gate signal is given, which means that the combined converter operates in the critical ZVS state. Furthermore, the ZVS operation of the switch S_4 is totally ensured at the critical state. These experimental results are consistent with the theoretical analysis in the previous section.

The experimental waveforms with step load are given in Fig. 14, where V_{bus_ac} and V_{out_ac} represent the ac compo-
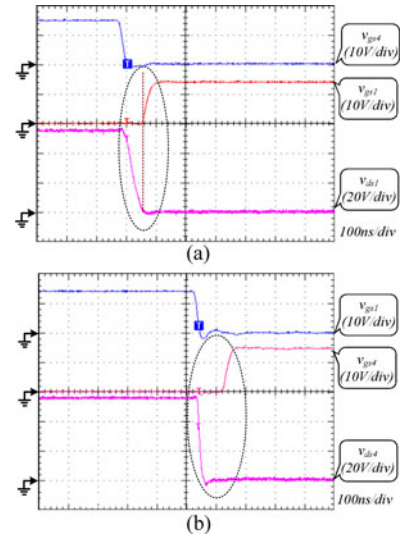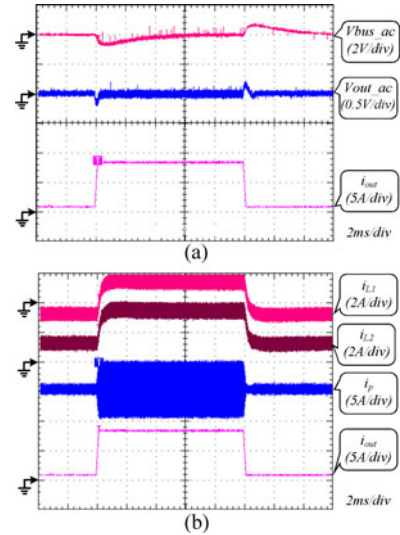
nents of the voltages V_{bus} and V_{out}. The secondary load varies from 0.833 to 8.33 A. It can be seen that the transient output voltage ripple is small even if a wide-range load variation occurs. And the dynamic response of the output voltage is fast although the PV output voltage V_{bus} is a little small with about 0.5 V voltage ripple. Due to the decoupled control of the PWM plus phase angle shift control scheme, the dynamic response of the bus voltage and the secondary output voltage is independent.

The efficiency of the derived converter is defined by

$$\eta = \frac{P_{out}}{P_{bus} + P_{bat}} \qquad (31)$$

where P_{out} is the secondary load power consumption, P_{bus} is the output power of the PV array, and P_{bat} is the provided or consumed power of the battery.
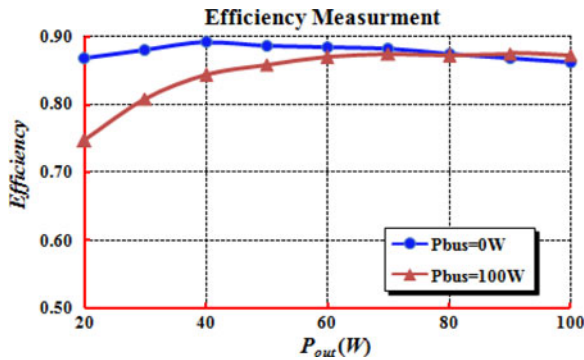
Fig. 15.   Efficiency measurement with different powers.

The efficiency curves of the combined three-port dc/dc converter with the proposed PPAS scheme when $P_{\rm bus} = 0$ and $P_{\rm bus} = 100\,{\rm W}$ are plotted in Fig. 15. When $P_{\rm bus} = 0$, which means that all the load energy is provided by the battery, the maximum efficiency is nearly 90% and the efficiency at 100-W full load is over 86%. When $P_{\rm bus} = 100\,{\rm W}$, which means that the battery is charged, the efficiency at 100-W full load is over 87%. According to the loss distribution analysis, the secondary diodes cover more than 50% of the total losses because the forward voltage of the used diode is nearly 1 V and the output voltage is only 12 V. The circuit efficiency can be improved by employing advanced synchronous rectification solution to greatly reduce the secondary conduction losses. Furthermore, the primary switch duty cycle is varied in the proposed converter to achieve the three-port voltage balance. This may slightly increase the primary switch conduction losses compared with the conventional full-bridge phase shift converter, where the duty cycle is always kept as 0.5. In addition, from the ZVS operation range analysis given in the previous section, the ZVS performance may be lost when the battery is in the charging mode, where the secondary load power is lower than the PV generated power. This also influences the conversion efficiency improvements.

VIII. Conclusion

In this paper, the switch duty cycle and the phase angle are employed as two decoupled and independent control freedoms within a certain operating range to achieve multiport energy conversion with high power device sharing ratio. This offers an innovative solution for multiport dc/dc converters to improve the design flexibility and enhance the power density. Furthermore, the bidirectional buck–boost converter and a full-bridge converter are combined together to generate a novel three-port circuit, which is adopted as an example to explore the clear advantages of the proposed scheme. All the primary switches can realize ZVS soft-switching performance under a certain load condition due to the proposed PPAS scheme. One of the main contributions of this paper is to illustrate the universal concept and considerations on the PPAS control scheme for combined three-port or multiport converters. The general control rule and the universal topology derivation law are proposed to explore novel multiport converters. The theoretical analysis and the experimental results have proved that the proposed PPAS scheme
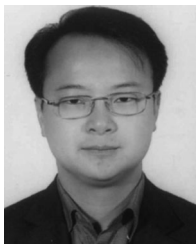
is an excellent candidate for multiport energy conversion systems.

References

[1] Q. Li and P. Wolfs, "A review of the single phase photovoltaic module integrated converter topologies with three different DC link configurations," *IEEE Trans. Power Electron.*, vol. 23, no. 3, pp. 1320–1333, May 2008.

[2] J. Selvaraj and N. A. Rahim, "Multilevel inverter for grid-connected PV system employing digital PI controller," *IEEE Trans. Ind. Electron.*, vol. 56, no. 1, pp. 149–158, Jan. 2009.

[3] L. Solero, A. Lidozzi, and J. A. Pomilio, "Design of multiple-input power converter for hybrid vehicles," *IEEE Trans. Power Electron.*, vol. 20, no. 5, pp. 1007–1016, Sep. 2005.

[4] A. A. Ferreira, J. A. Pomilio, G. Spiazzi, and L. de Araujo Silva, "Energy management fuzzy logic supervisory for electric vehicle power supplies system," *IEEE Trans. Power Electron.*, vol. 23, no. 1, pp. 107–115, Jan. 2008.

[5] B. G. Dobbs and P. L. Chapman, "A multiple-input DC–DC converter topology," *IEEE Power Electron. Lett.*, vol. 1, no. 1, pp. 6–9, Mar. 2003.

[6] N. D. Benavides and P. L. Chapman, "Power budgeting of a multiple-input buck–boost converter," *IEEE Trans. Power Electron.*, vol. 20, no. 6, pp. 1303–1309, Nov. 2005.

[7] A. Khaligh, J. Cao, and Y. J. Lee, "A multiple-input DC–DC converter topology," *IEEE Trans. Power Electron.*, vol. 24, no. 3, pp. 862–868, Mar. 2009.

[8] A. Al-Atrash, F. Tian, and I. Batarseh, "Tri-modal half-bridge converter topology for three-port interface," *IEEE Trans. Power Electron.*, vol. 22, no. 1, pp. 341–345, Jan. 2007.

[9] Z. Qian, O. Abdel-Rahman, H. Al-Atrash, and I. Batarseh, "Modeling and control of three-port DC/DC converter interface for satellite applications," *IEEE Trans. Power Electron.*, vol. 25, no. 3, pp. 637–649, Mar. 2010.

[10] Z. Qian, O. Abdel-Rahman, and I. Batarseh, "An integrated four-port DC/DC converter for renewable energy applications," *IEEE Trans. Power Electron.*, vol. 25, no. 7, pp. 1877–1887, Jul. 2010.

[11] A. Kwasinski, "Identification of feasible topologies for multiple-input DC–DC converters," *IEEE Trans. Power Electron.*, vol. 24, no. 3, pp. 856–861, Mar. 2009.

[12] Y. Li, X. Ruan, D. Yang, F. Liu, and C. K. Tse, "Synthesis of multiple-input DC/DC converters," *IEEE Trans. Power Electron.*, vol. 25, no. 9, pp. 2372–2385, Sep. 2010.

[13] Y. C. Liu and Y. M. Chen, "A systematic approach to synthesizing multiinput DC–DC converters," *IEEE Trans. Power Electron.*, vol. 24, no. 1, pp. 116–127, Jan. 2009.

[14] D. Liu and H. Li, "A ZVS bi-directional DC–DC converter for multiple energy storage elements," *IEEE Trans. Power Electron.*, vol. 21, no. 5, pp. 1513–1517, Sep. 2006.

[15] G. J. Su and L. Tang, "A multiphase, modular, bidirectional, triple-voltage DC–DC converter for hybrid and fuel cell vehicle power systems," *IEEE Trans. Power Electron.*, vol. 23, no. 6, pp. 3035–3046, Nov. 2008.

[16] J. L. Duarte, M. A. M. Hendrix, and M. G. Godoy, "Three-port bidirectional converter for hybrid fuel cell systems," *IEEE Trans. Power Electron.*, vol. 22, no. 2, pp. 480–487, Mar. 2007.

[17] H. Tao, J. L. Duarte, and M. A. M. Hendrix, "Three-port triple-half-bridge bidirectional converter with zero-voltage switching," *IEEE Trans. Power Electron.*, vol. 23, no. 2, pp. 782–792, Mar. 2008.

[18] H. Tao, A. Kotsopoulos, J. L. Duarte, and M. A. M. Hendrix, "Transformer-coupled multiport ZVS bidirectional DC–DC converter with wide input range," *IEEE Trans. Power Electron.*, vol. 23, no. 2, pp. 771–781, Mar. 2008.

[19] C. Zhao, S. D. Round, and J. W. Kolar, "An isolated three-port bidirectional DC–DC converter with decoupled power flow management," *IEEE Trans. Power Electron.*, vol. 25, no. 5, pp. 2443–2453, Sep. 2008.

[20] H. Krishnaswami and N. Mohan, "Three-port series-resonant DC–DC converter to interface renewable energy sources with bidirectional load and energy storage ports," *IEEE Trans. Power Electron.*, vol. 24, no. 10, pp. 2289–2297, Oct. 2009.

[21] H. Al-Atrash, M. Petter, and I. Batarseh, "A zero-voltage switching three-port isolated full-bridge converter," *IEEE Int. Telecom. Energy Conf.*, 2006, pp. 1–8.

[22] H. Al-Atrash and I. Batarseh, "Boost-integrated phase-shift full-bridge converter for three-port interface," *IEEE Power Electronics Specialists*, pp. 2313–2321, 2007.

[23] R. Kadri, J. P. Gaubert, and G. Champenois, "An improved maximum power point tracking for photovoltaic grid-connected inverter based on

voltage-oriented control," *IEEE Trans. Ind. Electron.*, vol. 58, no. 1, pp. 66–75, Jan. 2011.

[24] A. Safari and S. Mekhilef, "Simulation and hardware implementation of incremental conductance MPPT with direct control method using Cuk converter," *IEEE Trans. Ind. Electron.*, vol. 58, no. 4, pp. 1154–1161, Apr. 2011.

[25] O. Lopez-Lapena, M. T. Penella, and M. Gasulla, "A new MPPT method for low-power solar energy harvesting," *IEEE Trans. Ind. Electron.*, vol. 57, no. 9, pp. 3129–3138, Sep. 2010.

[26] B. Yang, W. Li, Y. Zhao, and X. He, "Design and analysis of a grid-connected PV power system," *IEEE Trans. Power Electron.*, vol. 25, no. 4, pp. 992–1000, Apr. 2010.

[27] W. Li, Y. Zheng, W. Li, Y. Zhao, and X. He, "A smart and simple PV charger for portable applications," in *Proc. IEEE Appl. Power Electronics Conf. Exposition*, 2010, pp. 2080–2084.

Yi Zhao (S'10) was born in Liaoning, China, in 1983. He received the B.Sc. degree from the College of Electrical and Electronic Engineering, Huazhong University of Science and Technology, Wuhan, China, in 2006, and is currently working toward the Ph.D. degree from the College of Electrical Engineering, Zhejiang University, Hangzhou, China.

His research interests include dc/dc converters and photovoltaic power system.

Wuhua Li (M'09) received the B.Sc. and Ph.D. degrees in applied power electronics and electrical engineering from Zhejiang University, Hangzhou, China, in 2002 and 2008, respectively.
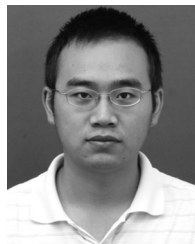
From September 2004 to March 2005, he was an Intern, and from January 2007 to June 2008, a Research Assistant in GE Global Research Center, Shanghai, China. From July 2008 to April 2010, he was with the College of Electrical Engineering, Zhejiang University, as a Postdoctoral Fellow. In May 2010, he became a faculty member at Zhejiang University as a Lecturer. In December 2010, he was promoted to Associate Professor. From July 2010 to September 2011, he was a Ryerson University Postdoctoral Fellow at the Department of Electrical and Computer Engineering, Ryerson University, Toronto, ON, Canada. He has published more than 70 technical papers and holds more than 20 issued/pending patents. His research interests include high-efficiency power converters and renewable energy power conversion system.
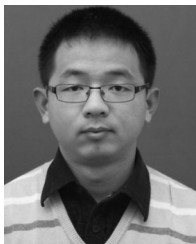
Jianguo Xiao was born in Zhejiang, China, in 1985. He received the B.Sc. and M.Sc. degrees in applied power electronics and power electronics and power drives from Zhejiang University, Hangzhou, China, in 2008 and 2011, respectively.

He is currently with GE (China) Research and Development Center Company, Ltd., Shanghai, China. His research interests include high-efficiency and high power-density converters for renewable systems.

Xiangning He (M'95–SM'96–F'10) received the B.Sc. and M.Sc. degrees from the Nanjing University of Aeronautical and Astronautical, Nanjing, China, in 1982 and 1985, respectively, and the Ph.D. degree from Zhejiang University, Hangzhou, China, in 1989.

From 1985 to 1986, he was an Assistant Engineer at the 608 Institute of Aeronautical Industrial General Company, Zhuzhou, China. From 1989 to 1991, he was a Lecturer at Zhejiang University. In 1991, he received a fellowship from the Royal Society of U.K., and conducted research in the Department of Computing and Electrical Engineering, Heriot-Watt University, Edinburgh, U.K., as a Postdoctoral Research Fellow for two years. In 1994, he joined Zhejiang University as an Associate Professor. Since 1996, he has been a Full Professor in the College of Electrical Engineering, Zhejiang University Hangzhou, China. He was the Director of the Power Electronics Research Institute and the Head of the Department of Applied Electronics, and he is currently the Vice Dean of the College of Electrical Engineering. He is the author or coauthor of more than 200 papers and one book: *Theory and Applications of Multi-level Converters* (China Machine Press, Beijing China). He holds 12 patents. His research interests include power electronics and their industrial applications.

Dr. He received the 1989 Excellent Ph.D. Graduate Award, the 1995 Elite Prize Excellence Award, the 1996 Outstanding Young Staff Member Award, and 2006 Excellent Staff Award from Zhejiang University for his teaching and research contributions. He received five Scientific and Technological Progress Awards from Zhejiang Provincial Government and the State Educational Ministry of China in 1998, 2002, and 2009, respectively, and five Excellent Paper Awards. He is a Fellow of the Institution of Engineering and Technology (formerly IEE), U.K.